

Cite this: *Nanoscale*, 2015, **7**, 6023

Understanding the conductive channel evolution in Na:WO_{3-x}-based planar devices†

Dashan Shang,^{*a,b} Peining Li,^a Tao Wang,^a Egidio Carria,^a Jirong Sun,^b Baogen Shen,^b Thomas Taubner,^{*a} Ilia Valov,^c Rainer Waser^{c,d} and Matthias Wuttig^{*a,d}

An ion migration process in a solid electrolyte is important for ion-based functional devices, such as fuel cells, batteries, electrochromics, gas sensors, and resistive switching systems. In this study, a planar sandwich structure is prepared by depositing tungsten oxide (WO_{3-x}) films on a soda-lime glass substrate, from which Na⁺ diffuses into the WO_{3-x} films during the deposition. The entire process of Na⁺ migration driven by an alternating electric field is visualized in the Na-doped WO_{3-x} films in the form of conductive channel by *in situ* optical imaging combined with infrared spectroscopy and near-field imaging techniques. A reversible change of geometry between a parabolic and a bar channel is observed with the resistance change of the devices. The peculiar channel evolution is interpreted by a thermal-stress-induced mechanical deformation of the films and an asymmetric Na⁺ mobility between the parabolic and the bar channels. These results exemplify a typical ion migration process driven by an alternating electric field in a solid electrolyte with a low ion mobility and are expected to be beneficial to improve the controllability of the ion migration in ion-based functional devices, such as resistive switching devices.

Received 22nd December 2014,
Accepted 25th February 2015

DOI: 10.1039/c4nr07545e
www.rsc.org/nanoscale

1. Introduction

The migration of ions in a solid electrolyte is a well-understood fundamental behavior of charge carrier species in solid electrolytes, and has been widely used in energy conversion and storage devices such as solid oxide fuel cells and batteries, and other smart devices like electrochromic windows and gas sensors.^{1–3} The control of ion migration in a solid electrolyte is very important to improve the device performance as well as to create novel physical and chemical functional devices. Recently, such coupled mass-charge transport along with the redox reaction at electrodes has led to explanations for resistive switching behaviors.^{4–8} In these devices, resistive switching employs localized conductivity changes by forming a conductive channel, usually called a filament, in the material bulk or

at the electrode/material interface. To fully understand the ion migration process in such devices, a detailed understanding of the dynamic channel evolution is mandatory. Many methods have so far been used to detect the conductive channels, such as scanning probe microscopy,^{9–12} *in situ* transmission electron microscopy,^{13–21} photo-emission electron microscopy,²² X-ray absorption spectroscopy,^{23,24} scanning electron microscopy,²⁵ and optical microscopy.^{26–29}

For the observed channel geometries, the dendritic shape is one of the typical configurations. The dendritic channels are usually metallic caused by reduction of cations (such as Ag⁺, Cu⁺).^{25,26} Their evolution mechanism is relatively well understood with some electrolytes, such as Ag/H₂O/Pt devices.²⁵ During the electroforming process, the Ag⁺ ions drift through the electrolyte and reduce to the Ag atom at the Pt electrode to form Ag dendritic channels which percolate the whole matrix to attain a low resistance state. The recent investigation indicates that the dendritic shape could be attributed to the high Ag⁺ ion mobility and low redox rate which result in the growth front at the tips moving faster than the surrounding and the interface morphologically unstable.³⁰ Reversing the applied electric field polarity, the channels usually break by the electrochemical dissolution of Ag atoms at the connective neck. Because of the low currents, the ion migration and therefore the channel formation are dominated by the electric field distribution in the matrix. When the ion mobility, such as oxygen ions, is relatively low in the matrix, the ion migration

^aI. Physikalisches Institut (IA), RWTH Aachen University, 52074 Aachen, Germany.

E-mail: taubner@physik.rwth-aachen.de, wuttig@physik.rwth-aachen.de

^bBeijing National Laboratory for Condensed Matter Physics and Institute of Physics, Chinese Academy of Sciences, Beijing 100190, China.

E-mail: shangdashan@iphy.ac.cn

^cInstitute für Werkstoffe der Elektrotechnik II, RWTH Aachen University, 52074 Aachen, Germany & Peter Grünberg Institute (PGI-7), Forschungszentrum Juelich, Juelich, Germany

^dJARA-FIT, Fundamentals of Future Information Technology, RWTH Aachen University, 52074 Aachen, Germany

† Electronic supplementary information (ESI) available. See DOI: 10.1039/c4nr07545e

requires a high electric field and substantial heating, and the conductive channel formation is thermal-assisted by the Joule heating effect. In this case, the dendritic characteristic of the channel is weakened and it shows other shapes such as a linear shape in a SrTiO₃ single crystal,⁹ cellular in Au/Fe:SrTiO₃/Au devices,³¹ conical in Pt/TiO₂/Pt device,¹⁵ dumbbell in Pt/Cr:SrTiO₃/Pt device,²³ trunk in Pt/ZnO/Pt device,²¹ and so on. Compared to the random nature of the dendritic channel, the above channels show a relatively regular shape and good scalability, providing more potential to control the channel geometry upon ion migration. However, a detailed understanding of the reversible ion migration processes, involving channels without obvious dendritic characteristic, is still lacking.

Tungsten oxide (WO_{3-x}) is one of the most important electrochromic materials.³ When a positive ion with a lower cation radius, such as H⁺, Li⁺, Na⁺, is injected into the material, together with an electron injection from the counter electrode, the valence of the tungsten ion is changed, forming an optical distinguished region in the material.³ Correspondingly, the conductivity of tungsten oxide will experience a low-to-high change.³ This unique property provides a tool for gaining insight into the ion migration process by detecting the evolution of the channel geometry and material conductivity. Here, we have investigated the dynamic channel geometry and resistance change of Na-doped WO_{3-x} films in a planar sandwich device. The entire evolution of the channels is observed using an *in situ* optical imaging technique combined with infrared spectroscopy. We found that the Na⁺ ion migration formed conductive channels, which shows different evolution behaviors from the reported dendritic channels. We have described the whole channel evolution through a thermal-stress-induced mechanical deformation and an asymmetric Na⁺ mobility distribution in the Na-doped WO_{3-x} films.

2. Experimental section

2.1. Device fabrication

Commercial soda-lime glass and quartz glass slides were used as substrates. WO_{3-x} films were deposited by pulsed laser deposition using a KrF excimer laser ($\lambda = 248$ nm) with a repetition rate of 1–5 Hz and a fluence of 5 J cm⁻². During the deposition, the substrate temperature was maintained at 673 K, and the oxygen pressure was kept at 10 Pa. The thickness of the films is about 100–500 nm. Au electrodes were deposited on top of the WO_{3-x} film by dc sputtering. The device sizes are 200 × 300 μm² and 100 × 150 μm² defined by photolithography and lift-off techniques. A thin cross-section lamella of 100 × 1000 × 5000 nm was cut by a focused ion beam (FIB, FEI Strata DB235) lift-out method. Scanning transmission electron microscopy (STEM, FEI Tecnai F20) and energy dispersive spectrometry (EDS, EDAX-Genesis) were carried out for the structure and composition analysis, respectively.

2.2. Electrical and optical measurements

Electrical property measurements were performed using a Keithley 2601 sourcemeter. Two metal probes were connected to the gold electrodes for applying the electric field and obtaining resistance measurements. Simultaneously, the spatially resolved color change of the sample was measured by illuminating it with light emitted from a halogen light source (MORITEX MHAA-100W) with a light output of 400–700 nm. The images were recorded by a computer-controlled complementary metal oxide semiconductor (CMOS) camera (ARTRAY-130MI) with a microscope lens.

2.3. Infrared measurements

The Fourier transform infrared (FTIR) reflectance spectra were taken with a Bruker Vertex 70 spectrometer in combination with a Hyperion 2000 infrared microscope. The objective used for the measurements has a 15 times magnification and its numerical aperture is 0.4. The FTIR spectra were recorded using a MCT (Mercury Cadmium Telluride) detector. During the experiments, knife-edge apertures were set to form a measurement area of about 20 × 20 μm². The background spectrum was measured with the same aperture size on the flat gold film as a reference. The spectra are normalized to this reference. The noise level of the spectra is corresponding to 200 scans with a resolution of 4 cm⁻¹.

The FTIR spectra were analyzed in the range from 900 to 2200 cm⁻¹ using SCOUT software. A layer stack as presented in Fig. 5a was simulated, with the dielectric data taken from Palik.³² The dielectric function $\varepsilon(\omega)$ of the WO_{3-x} film is composed of the following terms: (1) a constant ε_{∞} , which accounts for the polarizability in the higher energy range, (2) a Drude-type contribution for free carriers in the WO_{3-x} film (ω_p and γ are the plasma frequency and damping of the free-carrier oscillation), and (3) a Lorentz oscillator to describe the optical phonon contribution in the WO_{3-x} film (ω_{TO} , Ω_p , and Γ represent the frequency, oscillator strength and damping of the optical phonon).

$$\varepsilon(\omega) = \varepsilon_{\infty} - \frac{\omega_p^2}{\omega(\omega + i\gamma)} + \frac{\Omega_p^2}{\omega_{TO}^2 - \omega^2 - i\omega\Gamma} \quad (1)$$

To achieve a high-resolution infrared spectroscopic mapping of the conductive channels, we used scattering-type scanning near-field optical microscopy (s-SNOM, Neaspec GmbH),³³ in which a metallized tip of a tapping-mode atomic force microscope (AFM) was illuminated with a focused beam of a CO₂ laser ($\omega = 970$ cm⁻¹) and the backscattered light from the tip was collected, as sketched in Fig. 6a. The AFM tip (radius 30 nm) is vibrated with an amplitude of about 40 nm at a tapping frequency of 270 kHz. To suppress background scattering from the tip shaft and the sample, the detector signal is demodulated by higher harmonic n . Due to the high field-enhancement at the tip end, the scanning probe works as a strong near-field light source. This allows for simultaneously recording topography and near-field infrared images with 10 nm scale resolution.³³ Furthermore, the s-SNOM has a high

sensitivity towards the free-carrier concentration in doped semiconductors.^{34,35} This is because the s-SNOM amplitude signals from the semiconductors rely on the near-field resonant interaction between the tip and the collective free-carrier oscillations (surface plasmons), highly sensitive to the variations of the plasma frequency of free carriers.^{34,35}

3. Results and discussion

3.1. Composition and structural characterization of the WO_{3-x} film

Fig. 1a shows the STEM images of the cross-section of the as-prepared WO_{3-x} /soda-lime glass. The WO_{3-x} film shows a bi-layered structure because of different elemental contrasts. By EDS analysis (Fig. 1d), much of the sodium (Na) was found in the WO_{3-x} film, especially in the layer near to the WO_{3-x} film surface (Area 2). In addition, compared with the soda-lime glass bulk, the Na concentration on the soda-lime glass substrate surface (Area 4) is reduced. This Na distribution indicates that Na^+ ions in the soda-lime glass substrate diffused into the WO_{3-x} film, leaving a Na^+ depletion region near the WO_{3-x} /glass interface.

Fig. 1b and c show the high resolution TEM microscopy of the WO_{3-x} film out of the channel. The WO_{3-x} layer near the Pt side shows an amorphous structure, while the other layer

near the glass substrate is mainly polycrystalline. The amorphous layer near the Pt side could be formed by the FIB milling process.^{36,37} By selected area electron diffraction spectroscopy (Fig. 1e), Magnéli phases (W_3O_8 , $\text{W}_{18}\text{O}_{49}$, and $\text{W}_{19}\text{O}_{55}$) can be observed in Area 3.³⁸ Because the detection is performed in the as-prepared devices, it can be suggested that the Magnéli phases and Na^+ ion immersion are generated during the film deposition.

3.2. Optical characterization of the channel

Fig. 2a sketches our planar sandwich devices, consisting of a thin Na:WO_{3-x} film on a soda-lime glass, and two top gold electrodes. Upon applying a constant current of 3 mA for 10 seconds to the two top electrodes, a dark-color region with a parabolic shape grew from the cathode (left) toward the anode (right). We denote this region as the parabolic channel. Its formation was accompanied by a decrease of the device resistance from the initial state ($\sim 122 \text{ k}\Omega$) to the OFF state ($\sim 74 \text{ k}\Omega$). The relatively low initial resistance of the device might be caused by both the Magnéli phases which have higher conductivity than the stoichiometric tungsten oxide,³⁸ and the Na doping effect which brings extra free electron in the WO_3 conduction band.³⁹ By applying a reversed constant current of -3 mA for 1 second, a conductive channel with a bar shape protruded from the cathode (right) and then was pushed into the parabolic channel. Correspondingly, the

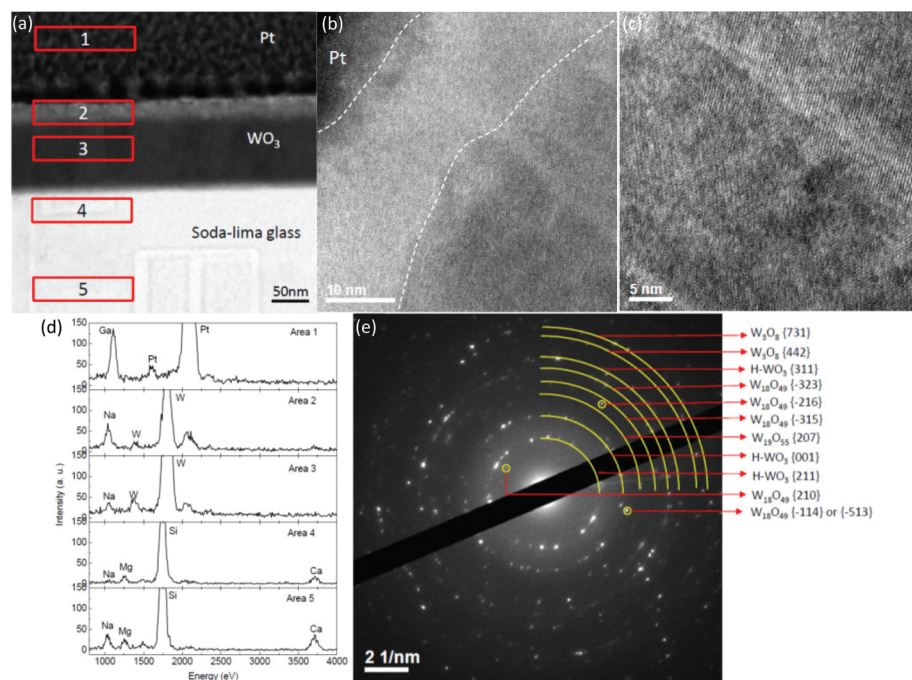


Fig. 1 (a) STEM images of the cross-section of the as-prepared WO_{3-x} /glass lamella. (b)–(c) High-resolution TEM images located in area 2 and area 3 in the panel (a). (d) Elementary composition analysis by EDS. Five regions, denoted by the red rectangles, were measured. The distribution of Na^+ ions confirms Na^+ ion immersion into the WO_{3-x} film during film preparation, leaving a Na^+ ion depletion region (area 4) in the glass substrate near the WO_{3-x} /glass interface. (e) Selected area electron diffraction of the WO_{3-x} film. The d -spacing calculated from the diffraction peaks and diffuse background confirm that the film consists of a mixture of crystalline hexagonal phase (H-WO_3), Magnéli phases (W_3O_8 , $\text{W}_{18}\text{O}_{49}$, and $\text{W}_{19}\text{O}_{55}$), and amorphous phase of tungsten oxide.

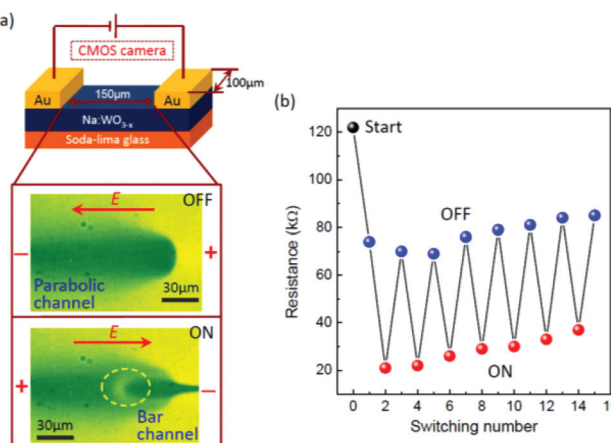


Fig. 2 Optical imaging of the conductive channel formation and the accompanying resistance switching. (a) Upper left side: schematic of the Au/WO_{3-x}/Au device structure. Lower left side: photo taken after applying current pulses (± 3 mA for 1 second). The arrows indicate the polarity direction of the applied electric field. (b) Resistance switching between the ON and OFF states by alternately changing the applied electric field polarity. The resistance is measured at 0.1 V after switching off the constant current. The device size is $100 \times 150 \mu\text{m}^2$.

device resistance decreased further to the ON state ($\sim 21 \text{ k}\Omega$). By reversing the current polarity, the bar channel shrunk back and the parabolic channel was restored. At the same time, the device resistance returned to the OFF state again ($\sim 70 \text{ k}\Omega$). By applying an electric field with a different polarity alternately, a reversible resistance switching between the ON and OFF state can be realized, accompanied by the appearance and disappearance of the bar channel.

For comparison, we applied the same current to a device with a quartz (SiO₂) glass substrate. However, no such color change can be observed from its optical image (see the ESI Fig. S1†). Moreover, no color change can be distinguished in the naked soda-lime glass substrate under the same experimental conditions. These results indicate that the channels we observed in the devices with soda-lime glass substrates are related to the existence of Na⁺ ions, which immerged into the WO_{3-x} films from the soda-lime glass substrate, as we have shown in Fig. 1.

Compared with the evolution of conductive channels reported before,^{18–26} there are two main differences in the channels formed by Na⁺ migration in the WO_{3-x} films. Firstly, we found that the parabolic channel cannot reach the right electrode (anode) to form percolation morphology, although we keep applying the electric field for a long time or increase the electric field. Instead, a slim channel always appears between the parabolic channel and the anode before the parabolic channel reaches the anode (see Fig. 3a–c), when the device resistance decreases abruptly from $\sim 110 \text{ k}\Omega$ to $78 \text{ k}\Omega$. From the SEM image (see Fig. 3f), it can be seen that a slim channel is formed by some new phases with dendritic shapes precipitated from the film. It is pointed out that this slim channel differs from the reported dendritic channels which

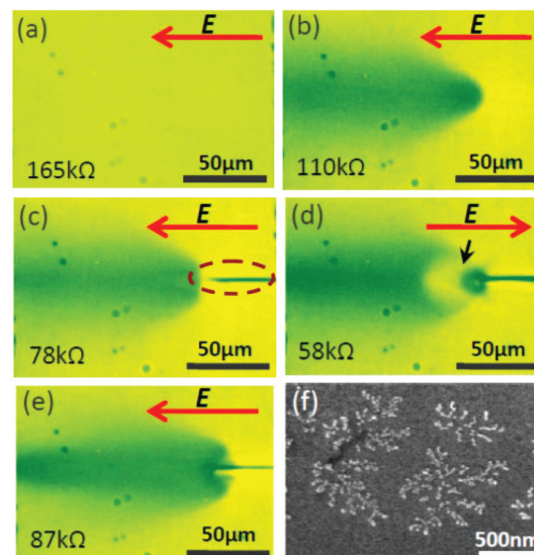


Fig. 3 (a)–(e) Optical images of slim channel formation and the following channel evolution: (a) Initial state. (b) The parabolic channel grew from the cathode by applying a constant current 2 mA for 10 seconds. (c) Slim channel formed in front of the parabolic channel, visible as a dark straight line (denoted by a dashed circle), after continuously applying the constant current for 25 seconds. Note that the slim channel formed under the same electric field polarity of the parabolic channel formation is different from that of bar channel formation. (d) ON state. A dark region appeared along the slim channel by applying -2 mA for 1 second. (e) OFF state. The parabolic channel was restored by applying 2 mA for 2 seconds. The slim channel became light and thin, but still existed. (f) SEM image on the region of the slim channel. The resistance values, marked at left bottom of the images, are measured at 0.1 V after switching off the constant current. The red arrows indicate the polarity direction of the applied electric field. The device size is $100 \times 150 \mu\text{m}^2$.

can be dissolved into the electrolyte under the reversed electric field.^{25,26} In contrast, the slim channel always exists on the film surface once it formed. As shown in Fig. 3d, when reversing the electric field polarity, a dark region formed around the slim channel at first, and then it dispersed, forming a connection with the parabolic channel, similar to that formed by the bar channel (see Fig. 2a), and the device resistance reduced to $58 \text{ k}\Omega$. Reversing the field polarity again, as shown in Fig. 3e, the parabolic channel was restored with the resistance increasing to $87 \text{ k}\Omega$. However, the slim channel, that is, the precipitated phases, still exists on the film surface.

Secondly, the connection between the parabolic channel and the bar channel is non-direct. A relatively “crescent-shaped” region, as shown by a dashed circle in Fig. 2a, always exists between the parabolic channel and the bar channel. In the rest of this paper, this peculiar connection is called a crescent-shaped connection to distinguish it from the direct connection by the conductive channels reported before.

The detailed dynamic processes involving the crescent-shaped connection/disconnection are investigated by measuring the real-time resistance change upon applying a constant

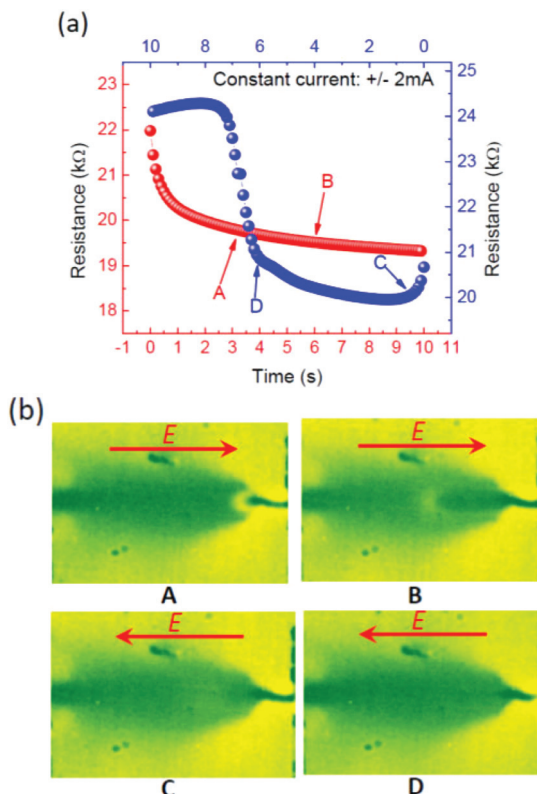


Fig. 4 (a) Real-time resistance change upon applying a constant current of ± 2 mA (red line) and 2 mA (blue line). (b) Corresponding images, taken simultaneously with the resistance measurement at times A, B, C, and D, shown in panel (a). The arrows indicate the polarity of the applied electric field. The device size is $200 \times 300 \mu\text{m}^2$.

current. The parabolic channel was formed firstly by applying a constant current of 2 mA. Then, the current direction was reversed before the slim channel formation. As shown in Fig. 4a, the device resistance decreases gradually under the negative electric field, corresponding to the bar channel protruding into the parabolic channel and forming the crescent-shaped connections (see the red line in Fig. 4a and picture A and B in Fig. 4b). Under the positive electric field, an interesting phenomenon is that the device resistance always decreases first to point C, and then increases slowly to point D, and then the device resistance increases sharply (see the blue line in Fig. 4a). This means the low-to-high resistance switching is not simply a monotonic process and the resistance change is dependent on the application time of the electric field. From the picture at point C in Fig. 4b, it can be seen that the crescent-shaped region disappears first. Nevertheless, the whole channel is still connected, indicating that the channel connection is not damaged but instead is improved. At point D, the disconnection of the channels occurs between the channel and the edge of the right electrode, resulting in a sharp increase of the device resistance. The entire connection/disconnection processes are shown as a movie in the ESI Movie S1.[†]

3.3. Infrared characterization of the channel

Infrared spectroscopy is widely used for the characterization of material properties such as electronic conductivity⁴⁰ and free-carrier densities.⁴¹ Because the optical response of free-carriers (Drude term contribution) has an obvious increase at low frequencies (infrared and below),⁴² the difference of free-carrier densities inside and outside the conductive channels should lead to a clear spectroscopic contrast in the infrared regime.

Fig. 5a shows FTIR spectra of the parabolic channel. It is seen that the spectra have a downward shift towards the baseline at wavenumbers above 1200 cm^{-1} , when the measured region moves from the center of the parabolic channel to the outside. This shift could be understood as the free-carrier density distribution in the conductive channel. To obtain the free-carrier density from these infrared spectra, the data are simulated with SCOUT (ref. 43), in which the complete optical

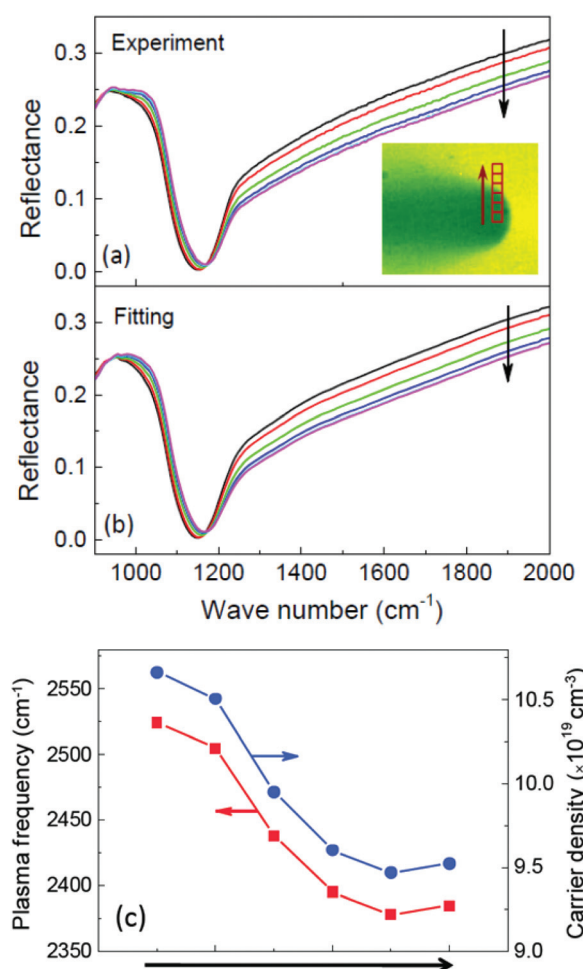


Fig. 5 FTIR measurement of the parabolic channel. (a) Measured and (b) simulated spectra. The measurement started from the center of the parabolic channel, as shown schematically in the inset, and moved towards the outside. For each measurement, an area of $20 \times 20 \mu\text{m}^2$ was measured. (c) Plasma frequency (ω_p) obtained by curve fitting and the resulting free carrier density.

system of the WO_{3-x} sample including the glass substrate is considered (see eqn (1)). The optimal parameters used for the fittings (Fig. 5b) are listed in the ESI Table S1.[†]

The contribution of free carriers in the WO_{3-x} layer is taken into account by a Drude term *via* a plasma frequency ω_p , which is given by

$$\omega_p^2 = \frac{ne^2}{\epsilon_0 m^*} \quad (2)$$

where n is the density of free carriers, e the electron charge, and m^* (~ 1.5 , ref. 44) the effective mass of the free carriers. The plasma frequencies and the resulting densities of free carriers are displayed in Fig. 5c. It can be seen that the free-carrier density in the channel is of the order of $10^{19}\text{--}10^{20} \text{ cm}^{-3}$ and decreases gradually from the center of the channel to the outside. The total density variation is about 15%.

The s-SNOM images of conductive channels are shown in Fig. 6c and d. In the image of the OFF-state (Fig. 6c), a bright parabolic region is clearly discernible, which corresponds to the parabolic channel observed in the optical microscope (Fig. 2a). In addition, some weak contrast bar channels adjacent to the parabolic channel are seen as well, which are hardly visible by optical microscopy. This could be ascribed to the small variation of free-carrier concentration in these additional channels (see the ESI Fig. S2[†]), which shows no distinguishable contrast in the visible range. Since they were formed before reversing the electric field, here we thus phrase them as “pre-formed” channels in order to distinguish them from the subsequent bar channel. In the infrared image of the ON state (Fig. 6d), it can be seen that the parabolic channel

nearly disappears upon reversal of the electric field. Instead, one of the pre-formed channels dominated in the image, forming the bar channel, as shown in Fig. 2a (ON state). No obvious topography change can be observed upon channel formation (Fig. 6b).

3.4. Model of the Na^+ migration processes in WO_{3-x} film

Based on above experimental evidence and analysis, a possible scenario for the Na^+ migration can be given to explain different channel evolution behaviors from the dendritic channels. Firstly, the soda-lime glass substrate serves as the Na^+ source. During the film deposition, Na^+ ions are introduced into the WO_{3-x} film from the substrate with a Na^+ -depleted layer formed beneath the WO_{3-x} film (see Fig. 1a). Driven by the external field, Na^+ ions in the films migrated towards the cathode, together with the counter electrons injecting into the film. This process corresponds to the electrochromic behavior of tungsten oxides and is described by the following chemical and the defect reactions:³⁹



In the channel forming process, the Na^+ source is blocked because the formed Na^+ -depleted layer insulates Na^+ in the substrate to be involved in the migration. Without the Na^+ source, the concentration of Na^+ near the anode soon decreases as they migrate towards the cathode. However, the cathode cannot serve as a sink because of the finite number of vacancies for Na^+ . Na^+ ions are therefore piled up at the cathode, and a Na^+ -enriched phase, *i.e.* the channel, grows from the cathode to the anode. In our previous results, we found that, for the films with different initial resistance values, the required electric power for the parabolic channel formation were almost constant,²⁸ providing evidence that the Na^+ migration is thermally-assisted. Thus, the channel shows a configuration different from the typical dendritic characteristic. By eqn (3), the proportion of low valence tungsten ions increases with increasing Na^+ concentration, and hence the number of color centers, leading to the color change of the film in the channel. Moreover, according to eqn (4), each ionized Na atom in Na_xWO_3 contributes simultaneously a cation located interstitially in a host WO_3 structure and an electron in the host conduction band. Correspondingly, the conductivity of the channel became higher due to the increase of free carrier concentration that has been demonstrated by the infrared measurements (see Fig. 5). Therefore, the parabolic channel growth implies the migration of the virtual cathode towards the anode.

With the growth of the virtual cathode, the electric field concentrated in front of it gradually, resulting in a high temperature in this region (see the ESI Fig. S4a-c[†]). The temperature difference could create appreciable thermal stress in the films. To a sufficient extent, the thermal stress induces mechanical deformation in the films, forming the pre-formed

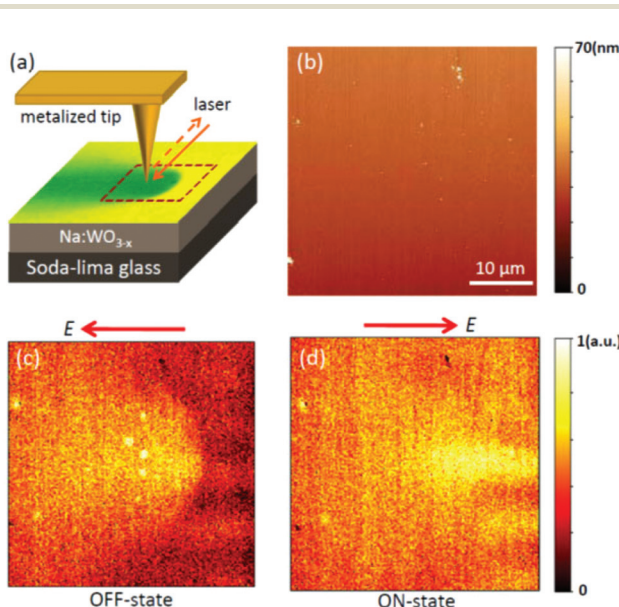


Fig. 6 The s-SNOM imaging. (a) Schematic of the s-SNOM set-up and the measured region. (b) Topography during the evaluation of conductive channels. The obtained near-field images of (c) the OFF-state and (d) the ON-state. The red arrows indicate the polarities of applied electric fields. The device size is $100 \times 150 \mu\text{m}^2$.

channel (Fig. 6c). The mechanical deformation could be too small to be detected from the change of film topography. Experimental evidence for the mechanical deformation origin of the preformed channel is that, on continuously applying the electric field, the pre-formed channel bulges out of the film before the slim channel formation (see the ESI Fig. S3†). On continuing application of the electric field before the parabolic channel reaches the anode, some thermal-chemical reaction occurs due to the extremely high temperature, forming the slim channel (Fig. 3f). Therefore, the parabolic channel could never reach the anode in our devices. The channel evolution from the pre-formed channel without topography change to the topography bulge, and then to the slim channel could be attributed to a consequence of different levels of thermal stress in the films with increasing temperature.

On reversing the electric field before the bulge deformation occurs, the Na^+ at the top of the parabolic channel moves first into the pre-formed channel. From the movement velocity of the top of the parabolic channels in six devices with the size of $200 \times 300 \mu\text{m}^2$, the ion mobility μ_p can be roughly estimated as $6.8 \times 10^{-7} \text{ cm}^2 \text{ V}^{-1} \text{ s}^{-1}$ according to the relation $l = \mu_p Vt/d$, where l is the distance over which the Na^+ moves ($\sim 102 \mu\text{m}$), V the applied voltage ($\sim 50 \text{ V}$), d the distance between the electrodes ($300 \mu\text{m}$), and t the required time ($\sim 8 \text{ s}$). By contrast, the ion mobility during the bar channel formation μ_b , estimated as $1.5 \times 10^{-5} \text{ cm}^2 \text{ V}^{-1} \text{ s}^{-1}$ with $l \sim 65 \mu\text{m}$, $V = 45 \text{ V}$, and $t = 0.3 \text{ s}$, shows a higher mobility than μ_p .⁴⁵ The higher Na^+ mobility in the pre-formed channel (or the bar channel later) might have been caused by the crystal defects induced by the mechanical deformation, such as the accumulation of crystallographic shear planes in the Magnéli phases with the lattice stress release under high thermal stress conditions. These defects could provide an effective pathway for the Na^+ migration. Due to the higher Na^+ mobility in the pre-formed channel (or the bar channel later), a Na^+ depletion region with a crescent-shaped appeared in the previous parabolic channel (Fig. 7b), as observed in Fig. 2a, 3d, and 4b. When reversing the electric field again, the Na^+ around the crescent-shaped region moved first because the electric and thermal field concentrated here at this moment (see the ESI Fig. S4d–f†), resulting in the crescent-shaped region being erased first (Fig. 7c). However, because Na^+ in the bar channel were not fully exhausted at that time, the bar channel was still connected with the electrode. Thus, a better connection between the parabolic and bar channel forms, corresponding to a small decrease of the device resistance, as observed in Fig. 4b (point C). With more Na^+ migrating out of the bar channel, the bar channel began to break from the electrode edge (Fig. 7d), as has been observed in Fig. 4b (point D). In a sense, the parabolic channel actually plays a role of a Na^+ reservoir, which supplies (stores) Na^+ moving into (out of) the bar channel.

It should be noted that, the magnitude of applied electric field estimated from the data in Fig. 2–3 is several ten kV cm^{-1} , which is 2–3 orders of magnitude lower than that for the metal ion migration in SiO_2 , which usually experiences an electric field of $\sim 1 \text{ MV cm}^{-1}$ for Ag and Cu and $3\text{--}5 \text{ MV cm}^{-1}$

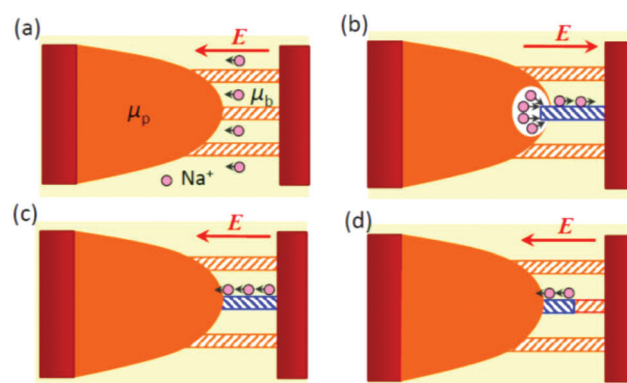


Fig. 7 Schematics illustrating the model for the conductive channel evolution with device resistance change. μ_p and μ_b are defined as the Na^+ mobility in the parabolic channel and the bar channel, respectively, with $\mu_p < \mu_b$. (a) Formation of the parabolic channel (orange region) and pre-formed channel (orange dashed region). (b) Bar channel formation (blue dashed region) along one of the pre-formed channels under reversed electric field. The shape of the parabolic channel also changes and forms a “crescent-shaped” connection with the bar channel. (c) Reversing the electric field again, the channel is restored to the parabolic shape firstly. (d) Subsequently the bar channel shrinks gradually from the right electrode side towards the parabolic channel.

for Ni and Pt.³⁰ The much lower driving field might be related to the defects in the WO_{3-x} films, such as the grain boundaries and the crystallographic shear planes in the Magnéli phases, which could provide the paths for short-circuit diffusion. To well understand the nature of ion migration in solid electrolyte with high defect concentration, further studies are still needed.

4. Conclusion

In summary, we have observed the entire process of the conductive channel evolution in Na^+ -doped WO_{3-x} films *via* an *in situ* optical imaging technique, infrared spectroscopy and near-field imaging. Different from the dendritic channels, the channel evolution shows a relevant geometric change between the parabolic channel and the bar channel. The pre-formation of the bar channel originates from the thermal-stress-induced mechanical deformation of the WO_{3-x} films. The crescent-shaped connection/disconnection processes are interpreted by the Na^+ migration with asymmetric ion mobility between the parabolic and the bar channel. These results give a typical example of a reversible ion migration in a solid electrolyte with low ion mobility and are expected to be beneficial to improve the controllability of the ion migration in ion-based functional devices, such as resistive switching devices.

Acknowledgements

We thank Roland Sittner and Manuel Bornhofft for the FIB and STEM measurement, Muhua Sun and Zhi Xu for the TEM

analysis, Yisheng Chai for the helpful discussion. The support from the collaborative research center ‘Nanoswitches’ (SFB 917) is acknowledged. D.S. acknowledges the support from the National Nature Science Foundation of China (grant no. 11274363 and 11134007) and the Alexander von Humboldt Foundation.

Notes and references

- 1 R. Mark Ormerod, *Chem. Soc. Rev.*, 2003, **32**, 17.
- 2 J. Maier, *Nat. Mater.*, 2005, **4**, 805.
- 3 G. A. Niklasson and C. G. Granqvist, *J. Mater. Chem.*, 2007, **17**, 127.
- 4 J. J. Yang, D. B. Strukov and D. R. Stewart, *Nat. Nanotechnol.*, 2013, **8**, 13.
- 5 R. Waser and M. Aono, *Nat. Mater.*, 2007, **6**, 833.
- 6 R. Waser, R. Dittmann, G. Staikov and K. Szot, *Adv. Mater.*, 2009, **21**, 2632.
- 7 A. Sawa, *Mater. Today*, 2008, **11**, 28.
- 8 K. Terabe, T. Hasegawa, T. Nakayama and M. Aono, *Nature*, 2005, **433**, 47.
- 9 K. Kzot, W. Speier, G. Bihlmayer and R. Waser, *Nat. Mater.*, 2006, **5**, 312.
- 10 I. Valov, I. Sapezanskaia, A. Nayak, T. Tsuruoka, T. Bredow, T. Hasegawa, G. Staikov, M. Aono and R. Waser, *Nat. Mater.*, 2012, **11**, 530.
- 11 M. H. Lee and C. S. Hwang, *Nanoscale*, 2011, **3**, 490.
- 12 D. S. Shang, L. Shi, J. R. Sun and B. G. Shen, *Nanotechnology*, 2011, **22**, 254008.
- 13 G. S. Park, Y. B. Kim, S. Y. Park, X. S. Li, S. Heo, M. J. Lee, M. Chang, J. H. Kwon, M. Kim, U. I. Chung, R. Dittman, R. Waser and K. Kim, *Nat. Commun.*, 2013, **4**, 2383.
- 14 Q. Liu, J. Sun, H. Lv, S. Long, K. Yin, N. Wan, Y. Li, L. Sun and M. Liu, *Adv. Mater.*, 2012, **24**, 1844.
- 15 D. H. Kwon, K. M. Kim, J. H. Jang, J. M. Jeon, M. H. Lee, G. H. Kim, X. S. Li, G. S. Park, B. Lee, S. Han, M. Kim and C. S. Hwang, *Nat. Nanotechnol.*, 2010, **5**, 148.
- 16 F. Miao, J. P. Strachan, J. J. Yang, M. X. Zhang, I. Goldfarb, A. C. Torrezan, P. Eschbach, R. D. Kelly, G. Medeiros-Ribeiro and R. S. Williams, *Adv. Mater.*, 2011, **23**, 5633.
- 17 J. Yao, L. Zhong, D. Natelson and J. M. Tour, *Sci. Rep.*, 2010, **2**, 242.
- 18 Y. Yang, P. Gao, S. Gaba, T. Chang, X. Pan and W. Lu, *Nat. Commun.*, 2011, **3**, 732.
- 19 Z. Xu, Y. Bando, W. Wang, X. Bai and D. Golberg, *ACS Nano*, 2010, **4**, 2515.
- 20 S. J. Choi, G. S. Park, K. H. Kim, S. Cho, W. Y. Yang, X. S. Li, J. H. Moon, L. J. Lee and K. Kim, *Adv. Mater.*, 2011, **23**, 3272.
- 21 J. Y. Chen, C. L. Hsin, C. W. Huang, C. H. Chiu, Y. T. Huang, S. J. Lin, W. W. Wu and L. J. Chen, *Nano Lett.*, 2013, **13**, 3671.
- 22 R. Yasuhara, K. Fujiwara, K. Horiba, H. Kumigashira, M. Kotsugi, M. Oshima and H. Takagi, *Appl. Phys. Lett.*, 2009, **95**, 012110.
- 23 M. Janousch, G. I. Meijer, U. Staub, B. Delley, S. F. Karg and B. P. Andreasson, *Adv. Mater.*, 2007, **19**, 2232.
- 24 J. P. Strachan, M. D. Pickett, J. J. Yang, S. Aloni, A. L. David Kilcoyne, G. Medeiros-Ribeiro and R. S. Williams, *Adv. Mater.*, 2010, **22**, 3573.
- 25 X. Guo, C. Schindler, S. Menzel and R. Waser, *Appl. Phys. Lett.*, 2007, **91**, 133513.
- 26 M. Kozicki and M. Mitkova, *J. Non-Cryst. Solids*, 2006, **352**, 567.
- 27 K. Azumi, K. Aoyama, S. Asanuma, Y. Uesu and T. Katsufuji, *Phys. Rev. B: Condens. Matter*, 2009, **79**, 121101.
- 28 D. S. Shang, L. Shi, J. R. Sun and B. G. Shen, *J. Appl. Phys.*, 2012, **111**, 053504.
- 29 D. S. Shang, J. R. Sun, B. G. Shen and M. Wuttig, *Chin. Phys. B*, 2013, **22**, 067202.
- 30 Y. C. Yang, P. Gao, L. Li, X. Pan, S. Tappertzhofen, S. H. Choi, R. Waser, I. Valov and W. D. Lu, *Nat. Commun.*, 2014, **5**, 4232.
- 31 C. Lenser, A. Kalinko, A. Kuzmin, D. Berzins, J. Purans, K. Szot, R. Waser and R. Dittmann, *Phys. Chem. Chem. Phys.*, 2011, **13**, 20779.
- 32 E. D. Palik, *Handbook of optical constants of solids*, Academic Press, San Diego, 1998.
- 33 R. Hillenbrand, T. Taubner and F. Keilmann, *Nature*, 2002, **418**, 159.
- 34 J. M. Stiegler, A. J. Huber, S. L. Diedenhofen, J. Gómez Rivas, R. E. Algra, E. P. A. M. Bakkers and R. Hillenbrand, *Nano Lett.*, 2010, **10**, 1387.
- 35 J. M. Stiegler, R. Tena-Zaera, O. Idigoras, A. Chuvalin and R. Hillenbrand, *Nat. Commun.*, 2012, **3**, 1131.
- 36 S. Rubanov and P. R. Munroe, *J. Microsc.*, 2004, **214**, 212.
- 37 L. A. Christel, J. F. Gibbons and T. W. Sigmon, *J. Appl. Phys.*, 1981, **52**, 7143.
- 38 D. B. Migas, V. L. Shaposhnikov and V. E. Borisenko, *J. Appl. Phys.*, 2010, **108**, 093714.
- 39 E. L. Runnerstrom, A. Llordés, S. D. Lounis and D. J. Milliron, *Chem. Commun.*, 2014, **50**, 10555.
- 40 J. H. Joo, R. Merkle, J. H. Kim and J. Maier, *Adv. Mater.*, 2012, **24**, 6507.
- 41 L. Ju, B. Geng, J. Horng, C. Girit, M. Martin, Z. Hao, H. A. Bechtel, X. Liang, A. Zettl, Y. R. Shen and F. Wang, *Nat. Nanotechnol.*, 2011, **6**, 630.
- 42 M. Fox, *Optical Properties in Solids*, Oxford University Press, UK, 2001.
- 43 W. Theiss, Detailed information about the simulation tool SCOUT. <http://wtheiss.com/>.
- 44 C. G. Granqvist, *Sol. Energy Mater. Sol. Cells*, 2000, **60**, 201.
- 45 The real mobility value should be larger than the estimated one because the growth of the bar channel is too fast to be captured by our camera.